

A comparison of different empirical potentials in ZnS

This content has been downloaded from IOPscience. Please scroll down to see the full text.

2014 Modelling Simul. Mater. Sci. Eng. 22 085014

(<http://iopscience.iop.org/0965-0393/22/8/085014>)

View [the table of contents for this issue](#), or go to the [journal homepage](#) for more

Download details:

IP Address: 129.128.32.56

This content was downloaded on 30/12/2014 at 00:33

Please note that [terms and conditions apply](#).

A comparison of different empirical potentials in ZnS

Mohammad Khalkhali, Qingxia Liu and Hao Zhang

Department of Chemical and Materials Engineering, University of Alberta, Edmonton, Alberta T6G 2V4, Canada

E-mail: hao.zhang@ualberta.ca

Received 14 July 2014, revised 29 September 2014

Accepted for publication 1 October 2014

Published 12 November 2014

Abstract

The accuracy of molecular dynamics simulation highly depends on the reliability of the empirical potential that it uses. Atomistic simulations of ZnS have attracted a lot of attention in the past few decades due to the technological importance of this material as a semiconductor and the main resource of world zinc production. Although multiple empirical potentials have been suggested for ZnS, there is no comprehensive study that compares the performance of these potentials. In this paper, we have reviewed five of the most used ZnS empirical potentials and have tested their performance in predicting different ZnS properties. Based on the obtained results, we provide recommendations for a proper empirical potential based on the application that the molecular mechanic simulation is aiming for.

Keywords: ZnS, empirical potentials, molecular dynamics

(Some figures may appear in colour only in the online journal)

1. Introduction

There are two main reasons for the technological importance of ZnS: (1) it is an important II–VI semiconductor, and (2) it is the main resource for the production of zinc metal. The former is due to the large direct band gap of ZnS that can be readily controlled by tailoring the structure and configuration of particles, especially in the nanoscale [1]. This property, which can lead to a wide range of optoelectronic applications, has been the motivation of various studies of ZnS nanostructures over the past few decades. Although the rapid growth of nanotechnology has enabled us to fabricate nanostructures with a variety of geometries, our understanding of their structural and configuration evolution is still limited. For ZnS nanostructures in particular, the uncontrollable changes in structure and configuration that can

occur in ambient conditions have been a challenging issue that questions the reliability of their use in optoelectronic applications [2]. The prediction of ZnS nanomorphology is inherently difficult experimentally because the thermodynamic properties of nanomaterials greatly differ from those of bulk materials [3]. In the past two decades, atomistic simulation methods have become important tools that compliment experimental studies by providing a fundamental understanding of the mechanisms of the structural and configurational evolutions in ZnS nanostructures. Some of the computational studies on ZnS nanostructures were reviewed by Hamad *et al* [4] and Feigl *et al* [2]. Several other works on ZnS nanostructures have studied the equilibrium configurations of nanoparticles [3, 5, 6] and nanowires [7], the effect of the environment [8, 9] and pressure [10] on structural transformation of nanoparticles, and the mechanical properties of ZnS nanowires and thin film [11].

ZnS mineral, sphalerite, is the primary source of zinc metal and is mainly recovered by the flotation process. Unlike most of the other sulfide minerals, sphalerite does not respond well to flotation. Therefore, sphalerite flotation requires activation by heavy-metal ions to enable adsorption of the collectors [12]. Although the activation of sphalerite has been surveyed extensively, conflicts still remain in regard to the mechanism of activation on the atomic scale. Computational studies of the ZnS activation process have mainly focused on the effect that the presence of activators have on the surface properties. The influence of the presence of lead [13] iron and copper [14, 15] species on (1 1 0) surface properties was studied using quantum mechanical methods. This technique is also reported in studies of the interaction of the collectors and activators on the sphalerite surface [16, 17].

Although atomistic simulation methods have so far proven to be promising approaches to address various problems, it should be kept in mind that their applicability is limited mainly by two factors: their accuracy in modelling interatomic interactions and their computational demands. Electronic structure methods based on quantum mechanic calculations are the most accurate available methods. The theory of quantum mechanics relies on the fact that energy and all other related properties of a system can be calculated by solving Schrödinger's equation. However, the exact solution of Schrödinger's equation is only feasible for the simplest systems. As a result, different electronic structure methods have been developed to estimate the solution of Schrödinger's equation by means of different mathematical approximations [18]. Despite all of the developments in hardware and software technologies, the computational expense of the first principle methods is still a crucial limitation that makes them technically impractical for systems beyond hundreds of atoms [19].

Molecular mechanic methods that use empirical potentials and laws of classical mechanics to model atomic interactions are the best alternative, offering a compromise between computational speed and accuracy [20]. Molecular dynamics (MD) simulations, in particular, enable the study of dynamics and atomic level evolutions of relatively large systems (up to millions of atoms or even more) in a practical time period (nanoseconds). This can result in the calculation of dynamic properties, such as heat and mass transfer, diffusion, surface absorption, and the geometry evolution of nanoparticles. MD can also be applied to derive the relations between thermodynamic quantities, namely: temperature, pressure, volume, and energy [21]. Overall, MD enables the study of systems and processes with more realistic dimensional and time scales. However, the accuracy of molecular mechanic methods is greatly dependent on the reliability of the empirical potential that they use to model the interatomic interactions. As a result, it is quite important to verify the reliability of empirical potentials by testing their ability to reproduce different material properties.

In this paper we focus on the five empirical potentials proposed for ZnS in the literature. Different material properties calculated using these potentials are compared with the corresponding experimental values or higher order first principle calculations. The ZnS

properties that are studied in this paper are important factors in the ZnS applications mentioned above. As a result, the ability to reproduce these properties can be considered to be good criteria to choose the appropriate empirical potential for computational studies of ZnS.

The five different potential functions of ZnS studied in this paper are developed by Wright and Jackson [22], Hamad *et al* [23], Wright and Gale [24], Grünwald *et al* [20] and Benkabou *et al* [25]. To avoid redundancy, we will name the potentials by their short terms as IP1, IP2, IP3, IP4 and IP5, respectively. The first four potential functions are based on the Born model of solids, which assumes that the interatomic potential of ionic-bonding materials consists of two main parts: long-range electrostatic and short-range energies. Thus, the potential energy for each atom can be written as:

$$U_i = \frac{1}{2} \sum_{j \neq i} \frac{q_i q_j}{4\pi\epsilon_0 r_{ij}} + \frac{1}{2} \sum_{j \neq i} V_{ij}(r_{ij}) + \text{multibody potentials}, \quad (1)$$

where the first and second terms are Coulomb and pair potentials. The Ewald summation method [26] is used in this paper to evaluate the long-range Coulombic interactions. The Shell model is also used in the first three potentials to add the prioritization effect. The shell model, proposed by Dick and Overhauser [27], defines a simple mechanical description to handle polarization. In this model, ions are considered to have two parts: the core, which carries atomic mass, and the shell, which takes the polarizable charge. The core and shell are connected by a spring so that the shell can displace from the core to model polarizability. The sum of the core and shell charges represents the total charge of ion and they interact with harmonic spring potential [28]:

$$V_{\text{core-shell}} = \frac{1}{2} k_s r^2. \quad (2)$$

In a potential developed by Benkabou *et al*, a totally different approach than the Born model is applied. In this approach, the parameters of the Tersoff potential [29, 30], which is based on the bond ordering concept, are optimized to reproduce the structural and mechanical properties of ZnS. These parameters are just introduced for Zn–S pairs, and Zn–Zn and S–S interactions have not been taken into account.

Among the empirical potentials studied in this paper, IP1 and IP2 have been repeatedly used in molecular dynamics and lattice dynamics simulations. IP1 has been used to study the surface properties of ZnS [6, 31], mechanical properties of ZnS nanowires and thin films [11], the structural evolution of ZnS nanoparticles in vacuum [6], in the presence of water [8] and during aggregation [32]. IP2 has also applied to study the structure of ZnS surfaces [23], nanoclusters and nanoparticles [33, 34] and embryonic growth in aqueous solution [35]. A more thorough version of IP3 that also includes two-body parameters for Fe–S and Mn–S interactions has been used to investigate the mechanisms of uptake and incorporation of cadmium, iron and manganese impurities in sphalerite via lattice dynamics surface studies [36]. The pressure induced phase transformation in CdSe/ZnS core/shell nanocrystals has been modelled via molecular dynamics study that implemented IP4 [10].

2. Structural and mechanical properties

The structural and mechanical properties of ZnS were calculated using different interatomic potential formulations and compared with the experimental values. These properties are the main material characteristics used in the derivation of interatomic potentials. In the other words, the potential parameters are optimized to fit the calculated properties to the experimental ones. A powerful force field is able to predict more material properties, especially those that are not used in the process of deriving potential parameters.

In potential derivation procedures, the lattice parameters that minimize the total energy of the system are usually optimized by fitting to experimental values. Experimental values are usually obtained at room temperature while the physical meaning of energy minimization is to lower the temperature to 0 K. However, this process is commonly acceptable because the thermal expansion in solids is negligible at low temperatures.

There are two main approaches to calculate elastic constants via atomistic simulation methods: (1) a method based on strain (or stress) fluctuations, and (2) a direct method that calculates elastic constants from stress–strain relation of material subjected to an external load. Fluctuation methods are based on the fact that elastic constants are equal to the second derivatives of the deformation energy with respect to strain:

$$\sigma_{ij} = \frac{\partial U}{\partial \epsilon_{ij}} \Rightarrow C_{ij} = \frac{\partial^2 U}{\partial \epsilon_i \partial \epsilon_j}, \quad (3)$$

where U , ϵ , σ and C_{ij} are deformation energy, strain, stress and corresponding elastic constant, respectively. Thus, the elastic stiffness matrix can be calculated by subjecting the structure to 12 deformations (3 pair of uniaxial and three pairs of pure shear) in a way in which each deformation constructs a small fluctuation along one strain vector while keeping the rest 0 [37].

In the direct method, elastic constants are achieved via constant pressure molecular dynamics. External pressure is applied in different directions to calculate the corresponding elastic moduli. The major advantage of the direct method is that it is potentially capable of considering the dynamics of the system. However, the variation of strain and stress during molecular dynamics simulations makes it necessary to use average values to calculate stress–strain behaviour. Consequently, one needs to run long simulations and make sure that strain equilibrates before each step of the stress [38].

In this study we have used GULP code [37], which applies the fluctuation method within the lattice dynamics calculations. The lattice constant values at 300 K and 0 GPa are also calculated using constant pressure molecular dynamic simulation within DL_POLY classic code [39]. Details of MD simulations are explained in section 6. Although some of the lattice constant and mechanical properties are reported for these potentials in their original papers, we have recalculated all of the structural and mechanical constants. This helps us to provide more consistent comparison between different potentials.

Three different crystal structures have been reported for ZnS in literature. Under standard conditions, ZnS can adopt two crystal structures, which are zinc-blende (ZB: $F43m$) and wurtzite (WZ: $P6_3mc$). Due to the similarity of unit cell volume and bond lengths, there is a small energy difference between these two structures. At higher pressures, the high density rocksalt structure (RS: $Fm3m$) becomes more stable. Table 1 shows the calculated lattice and mechanical constants for three ZnS phases for each potential. The values reported in the original papers (numbers in parentheses) and corresponding experimental results are also represented where available. Since the rocksalt phase is not stable in standard conditions, the experimental value for lattice constant of this structure has been calculated by extrapolating the lattice volume at higher pressures to 0 GPa [40].

As seen in table 1, there is a wide range of experimental data values for mechanical properties. Since mechanical properties are one of the main parameters used in the derivation of empirical potentials, the values calculated by each potential are strictly dependent on the corresponding experimental values used in the derivation process. There are a few noticeable differences between mechanical properties calculated in this study and those reported in original papers, which is likely due to the use of different calculation methods. Keeping in mind the inherent uncertainty of the experimental results, the IP2 potential seems to have a

Table 1. Comparison of mechanical and structural properties calculated via different potentials of ZnS (lattice parameters are in Å and mechanical properties are in GPa).

	IP1	IP2	IP3	IP4	IP5	exp.
ZB						
<i>a</i>	5.403 (5.407)	5.410 (5.41)	5.450 (5.45)	5.475 (5.48)	5.367 (5.406)	
<i>a</i> (300 K)	5.401	5.431	5.459	5.501	—	5.409 ^a , 5.412 ^b , 5.41 ^c
<i>C</i> ₁₁	91.834 (91.7)	105.563 (105.1)	107.060 (107.1)	106.200 (150.1)	98.435 (98.0)	107.1 ^d , 104.6 ^e , 94.2 ^c
<i>C</i> ₁₂	58.285 (58.2)	67.727 (67.8)	59.821 (59.4)	73.386 (51.4)	80.949 (73.0)	66.7 ^d , 65.3 ^e , 56.8 ^c
<i>C</i> ₄₄	60.103 (44)	42.909 (43.1)	32.977 (33.2)	51.740 (62.2)	20.019	46.55 ^d , 46.13 ^e , 43.6 ^c
<i>B</i>	69.468	80.339 (80)	75.128 (75.6)	84.324 (83.4)	86.778 (81.6)	74.8 ± 3.2 ^f , 79.5 ^g
WZ						
<i>a</i>	3.867 (3.91)	3.876 (3.87)	3.894 (3.89)	3.895 (3.89)	3.795	
<i>a</i> (300 K)	3.824	3.851	3.889	3.863	—	3.816 ^g , 3.85 ^c , 3.8230 ^k
<i>c</i>	6.092 (6.05)	6.088 (6.10)	6.191 (6.20)	6.241 (6.26)	6.198	
<i>c</i> (300 K)	6.247	6.291	6.312	6.353	—	6.252 ^g , 6.29 ^c , 6.2565 ^k
<i>C</i> ₁₁	124.556 (108.5)	124.720 (124.2)	110.722 (111.3)	130.568 (161.4)	107.444	124.2 ^h , 122.2 ⁱ , 131.2 ^c
<i>C</i> ₁₂	46.349 (54.9)	60.092 (59.8)	55.733 (55.6)	68.052 (53.8)	79.442	60.15 ^h , 59.1 ⁱ , 66.3 ^c
<i>C</i> ₁₃	42.484 (53.2)	59.092 (58.0)	58.739 (57.9)	56.769 (28.2)	73.426	45.54 ^h , 46.0 ⁱ , 50.9 ^c
<i>C</i> ₃₃	115.389 (86.8)	113.211 (113.0)	124.195 (126.4)	137.103 (213.1)	113.471	140.0 ^h , 138.5 ⁱ , 140.8 ^c
<i>C</i> ₄₄	40.270 (26.8)	37.403 (37.3)	37.525 (37.7)	32.459 (32.4)	12.504	28.64 ^h , 28.23 ⁱ , 28.6 ^c
<i>C</i> ₆₆	39.103 (34.4)	32.314	27.496	31.258 (53.8)	14.001	32.03 ^h , 32.4 ^c
<i>B</i>	69.519	79.713	76.560 (76.4)	84.582 (82.3)	86.772	80.1 ^g , 75.8 ^j
RS						
<i>a</i>	5.075	5.050	5.376	5.194 (5.20)	4.754	5.06 ^b
<i>C</i> ₁₁	122.560	127.818	228.319	108.697 (73.2)	501.082	—
<i>C</i> ₁₂	77.298	81.177	76.840	88.973 (45.3)	0.000	—
<i>C</i> ₄₄	77.298	96.671	67.046	88.973 (45.3)	11.522	—
<i>B</i>	92.385	96.724	127.333	95.548 (54.6)	167.027	103.6 ^b

^a Ref. [41], ^b Ref. [40], ^c Ref. [42], ^d Ref. [43] (77 K), ^e Ref. [43] (298 K), ^f Ref. [44], ^g Ref. [45], ^h Ref. [46], ⁱ Ref. [47], ^j Ref. [48], ^k Ref. [60].

better overall agreement with the experimental lattice constants and the mechanical properties of the three ZnS phases.

As expected, all of the potentials overestimate the 300 K lattice constant of zinc-blende phase since the experimental results (which are obtained in room temperature) are fitted to those calculated via energy minimization. However, almost all of the potentials can reproduce experimental wurtzite lattice constants at 300 K. It can be seen that wurtzite lattice constant a is overstimulated by energy minimization while c is underestimated. Nevertheless, increasing temperature causes the lattice constant to approach their experimental values. One improvement which can easily be applied to potential derivation methods uses lattice constants calculated by NPT MD simulations at 300 K and 0 GPa in the optimization procedure instead of those obtained via energy minimization.

Three-body potentials have a very short range nature and usually do not go further than the first neighbour atomic distance. Considering a Zn atom, the first, second, third and fourth neighbours are S, Zn, S, Zn atoms at $\frac{\sqrt{3}}{4}a$, $\frac{\sqrt{2}}{2}a$, $\frac{\sqrt{10}}{4}a$ and a distances, where a is the lattice constant. In the case of zinc-blende ZnS ($a = 5.41$), the first, second, third and fourth neighbour distances would be 2.343 Å, 3.825 Å, 4.277 Å and 5.41 Å, respectively. The atomic distances in wurtzite are similar to zinc-blende because of their alike densities. Therefore the cut-off distance of 6 Å, which was proposed for IP3 potential, seems to be too high for three-body interactions because it goes beyond the fourth neighbour. The effect of the high three-body cut-off is noticeable in rocksalt ZnS, which is a more compact phase. As can be seen in table 1, there is a large difference between rocksalt properties calculated by IP3 and other potentials. We have tried different three-body cut-offs for the IP3 potential without changing the formulation itself and results are given in table 2.

Table 2 shows that changing three-body cut-offs improves rocksalt properties predicted by IP3 potential. Except for C_{11} and C_{33} of wurtzite, which become softer, it seems that changing three-body cut-off has no significant effect on other properties of zinc-blende and wurtzite phases.

Using the shell model inherently causes MD simulations to become more complicated. Firstly, the shell model introduces a new species into the system, which will increase the simulation time. Additionally, handling shells in MD simulations requires more care, especially in higher temperatures and pressures. We will discuss the MD simulation of the shell model in section 6. Adding many-body terms in potential formulations can also slow down MD simulations. This made us interested in investigating how removing the shell model and four-body term affects the material properties predicted by IP2 and IP3 potentials. Table 3 compares the structural and mechanical properties before and after removing shell model and four-body term from IP2 and IP3 potentials.

Table 3 clearly shows that omitting the four-body potential from the IP3 formulation does not significantly affect the structural and mechanical properties. On the other hand, removing the shell model does show a noticeable effect on wurtzite and zinc-blende properties for both potentials. In some cases, (IP2: zinc-blende C_{44} and wurtzite C_{11} , C_{44} and C_{66} , IP3: zinc-blende C_{44} and wurtzite C_{12} , C_{44} and C_{66}) removing the shell model results in deviations from the experimental values while other cases (IP2: wurtzite C_{13} , C_{33} , IP3: wurtzite C_{11} , C_{13} and C_{33}) approach to experimental values after removing the shell model.

3. Phonon dispersion

The calculation of phonon dispersion spectra in solid crystals is interesting because it can be used to obtain some material properties, such as heat capacity, thermal expansion coefficient

Table 2. Effect of changing three-body cut-off on structural and mechanical properties calculated via IP3 potential (lattice parameters are in Å and mechanical properties are in GPa).

	Zn-S 6.0 Å	Zn-S 3.0 Å
ZB		
<i>a</i>	5.450	5.441
<i>C</i> ₁₁	107.060	104.636
<i>C</i> ₁₂	59.821	58.180
<i>C</i> ₄₄	32.977	32.907
<i>B</i>	75.128	73.665
WZ		
<i>a</i>	3.894	3.902
<i>c</i>	6.191	6.110
<i>C</i> ₁₁	110.722	107.221
<i>C</i> ₁₂	55.733	55.219
<i>C</i> ₁₃	58.739	58.314
<i>C</i> ₃₃	124.195	109.103
<i>C</i> ₄₄	37.525	40.604
<i>C</i> ₆₆	27.496	26.002
<i>B</i>	76.560	74.100
RS		
<i>a</i>	5.376	5.200
<i>C</i> ₁₁	228.319	140.585
<i>C</i> ₁₂	76.840	96.586
<i>C</i> ₄₄	67.046	79.523
<i>B</i>	127.333	111.252

and phonon–electron interaction. Phonon–electron interaction is especially attractive in semiconductor materials like ZnS because it can govern the optoelectronic properties. Phonon dispersion data is also one of the material properties that can be readily used in empirical interatomic potential development. Since phonon data was not used as a fitting parameter in developing any of the potentials mentioned in this study, the ability of each potential to reproduce the experimental data can be a good way to test them.

In this section, the experimental phonon dispersion data of zinc-blende and wurtzite ZnS is compared with those calculated via empirical potentials. Phonon dispersion calculations were performed using the module within GULP software and the experimental results were obtained from Raman scattering study of Cheng *et al* [49]. The details of the calculation process can be found elsewhere [37]. However, it is important to mention that the calculation of Born effective charge and high frequency dielectric constant tensor is necessary in ionic materials to add a correction that is responsible to break the degeneracy of the transverse optical (TO) and longitudinal optical (LO) modes. Thus, these tensors are calculated for each potential formulation and they are represented in table 4, along with the corresponding experimental values.

Table 4 shows that IP1 potential underestimates ZnS ionicity compared to the experimental results. As mentioned above, the Born effective charge of IP4 ZnS, which does not include the shell model, is equal to the nominal charge of the cores. Atoms are not charged in IP5, so the

Table 3. Comparison of mechanical and structural properties calculated by IP2 and IP3 potential with and without shell model and four-body potential (lattice parameters are in Å and mechanical properties are in GPa).

	IP2 (No Shell)	IP2	IP3 (No 4-bd)	IP3 (No Shell)	IP3
ZB					
<i>a</i>	5.410	5.410	5.450	5.450	5.450
<i>C</i> ₁₁	105.563	105.563	107.060	107.060	107.060
<i>C</i> ₁₂	67.727	67.727	59.821	59.821	59.821
<i>C</i> ₄₄	64.950	42.909	32.977	65.652	32.977
<i>B</i>	80.339	80.339	75.128	75.567	75.128
WZ					
<i>a</i>	3.868	3.876	3.894	3.888	3.894
<i>c</i>	6.116	6.088	6.191	6.209	6.191
<i>C</i> ₁₁	140.254	124.720	110.719	133.816	110.722
<i>C</i> ₁₂	55.883	60.092	55.716	43.691	55.733
<i>C</i> ₁₃	49.321	59.092	58.695	43.615	58.739
<i>C</i> ₃₃	131.596	113.211	124.227	137.704	124.195
<i>C</i> ₄₄	42.264	37.403	37.537	46.837	37.525
<i>C</i> ₆₆	42.185	32.314	27.501	45.350	27.496
<i>B</i>	79.932	79.713	76.540	76.609	76.560
RS					
<i>a</i>	5.050	5.050	5.376	5.376	5.376
<i>C</i> ₁₁	127.818	127.818	228.316	228.319	228.319
<i>C</i> ₁₂	81.177	81.177	76.816	76.840	76.840
<i>C</i> ₄₄	96.671	96.671	67.048	67.046	67.046
<i>B</i>	96.724	96.724	127.316	127.333	127.333

Table 4. Born effective charges and high frequency dielectric constants.

	IP1	IP2	IP3	IP4	IP5	exp.
ZB						
<i>Z</i> _{xx} [*]	0.66	1.82	1.46	1.18	—	2.15 ^a
<i>ε</i> _{zz} [∞]	4.14	3.35	4.9	—	—	5.2 ^b , 4.4 ^c
WZ						
<i>Z</i> _{xx} [*]	0.63	1.80	1.44	1.18	—	
<i>Z</i> _{zz} [*]	0.72	1.86	1.55	1.18	—	
<i>ε</i> _{xx} [∞]	4.01	3.32	4.82	—	—	
<i>ε</i> _{zz} [∞]	4.43	3.41	5.09	—	—	

^a Ref. [50], ^b Ref. [51], ^c Ref. [52].

Born effective charge cannot be defined. For both IP1 and IP4, the dielectric constant tensor is equal to the unit matrix. Using the information calculated in table 4, phonon dispersion relation for zinc-blende and wurtzite phases are calculated and shown in figures 1. Phonon band structures are drawn along ΓX and ΓA directions for ZB and WZ structures, respectively, where Γ , X and A are high symmetry points in the Brillouin zone. Γ refers to the centre

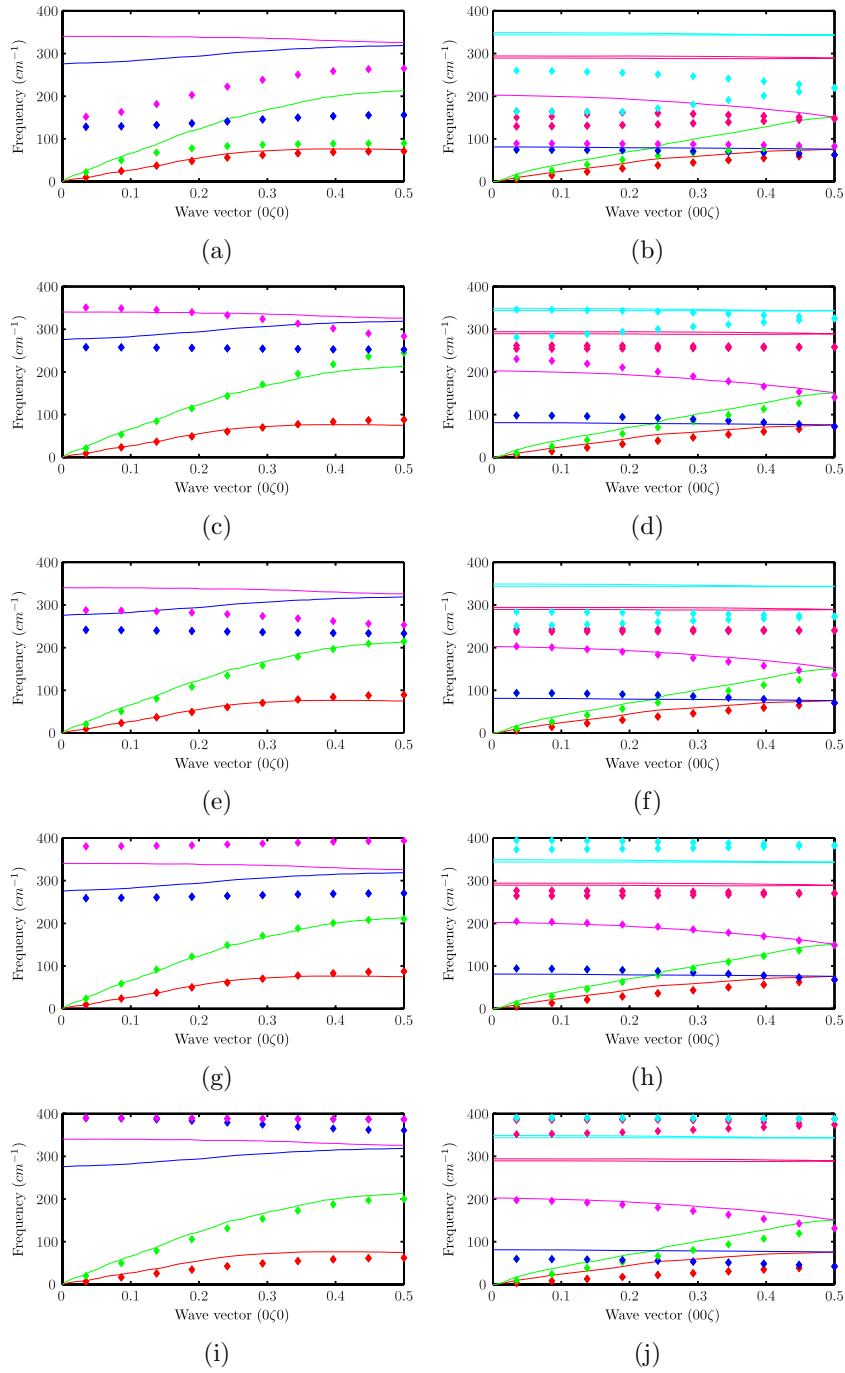


Figure 1. Phonon dispersion relations of ZnS calculated with (a) and (b) IP1, (c) and (d) IP2, (e) and (f) IP3, (g) and (h) IP4, and (i) and (j) IP5. Right and left figures are correspond to zinc-blende and wurtzite phases, respectively. The solid lines represent the experimental results taken from [49] and the filled circles are calculated phonon frequencies.

of the Brillouin zone ($k = 0, 0, 0$) while X and A are $k = 0, \frac{1}{2}, 0$ and $k = 0, 0, \frac{1}{2}$ in the corresponding Brillouin zones of zinc-blende and wurtzite structures, respectively. In figure 1, the solid lines represent the experimental results that were obtained from the Raman scattering study of Cheng *et al* [49] and the filled diamonds are the values calculated using the interatomic potentials.

Except for IP1, the acoustic phonons calculated using the empirical potentials are in good agreement with the experiment. All of the potentials show weakness in the calculation of optic phonons. This is worse for IP5 because there is no LO/TO splitting in Γ point. As pointed out by Wright and Gale [24], this happens because of the fact that species do not carry charge in IP5. Among the other three, it seems that the IP2 potential can reproduce better Γ point phonon frequencies for zinc-blende ZnS. The phonon dispersion relations obtained by IP4 also show an acceptable agreement to the experimental values, despite its simple formulation.

4. Surface energy and structure

There is a considerable number of studies on the surface properties of ZnS using first principle and molecular mechanics methods. The high surface to volume ratio in nanostructures makes the surface properties a crucial topic in nanoscience. As a result, the ability of an interatomic potential in predicting surface properties can be an important factor for using it in nanoscience.

The energy penalty to cleave a bulk material and form a surface is defined as the surface energy. By this definition, the surface energy for any stable material is a positive value (making a free surface is endothermic) and can be calculated as:

$$E_s = \frac{[U_s - nU_{\text{coh}}]}{A}, \quad (4)$$

where E_s is surface energy, U_s is the energy of the system that contains the surface, n is number of atoms in the same system, U_{coh} is the cohesive energy per atom in periodic bulk system and A is the surface area.

There are two main approaches for calculating surface energy by atomistic simulation methods. In the first method, which we call the 3D method, a system with two free surfaces is made by introducing vacuum gaps. This can be done by increasing the simulation cell length along one axis, making a slab with two free surfaces normal to the increased dimension. It should be kept in mind that the simulation is still running in a 3D periodic environment, so that the vacuum gap should be sufficiently large to avoid the interaction of the free surfaces with their images. The slab itself should be thick enough to ensure that properties converge to bulk properties at the centre of the slab. The advantage of the 3D method is that it can be used with codes that can only handle 3D boundary conditions. This is crucial, especially when there is long range electrostatic interaction in the system (like ZnS), since many of the available MD codes have not implemented the two-dimensional Ewald summation. The main disadvantage of this method is the necessity of a larger simulation box due to the presence of vacuum gaps, which will increase the simulation time.

In the second method (2D method), a system with a single surface and two regions is made. Region 1 contains the surface and all of the layers below the surface are allowed to relax. The atoms in region 2 are assumed to have no displacement from the relaxed bulk structure. The 2D method is more efficient and an ionic system was made possible by introducing the 2D version of the Ewald summation that was developed by Parry [53] (known as Parry summation).

We used both methods within GULP code to calculate (1 1 0) the surface energy of zinc-blende ZnS. Since both methods produced similar results for all of the potentials, we have used a 2D method to calculate other surface energies. (1 1 0) is found to be the most stable surface

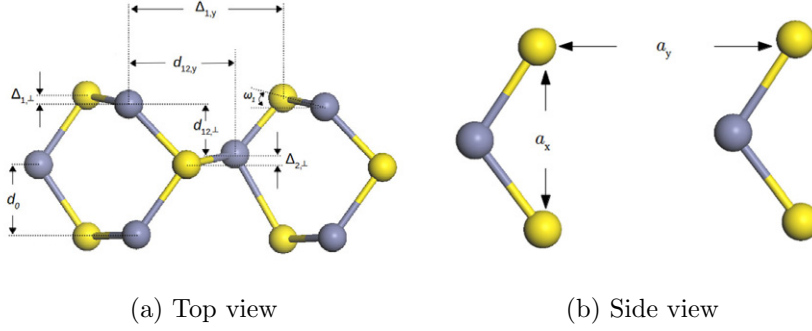


Figure 2. Side and top views of the relaxed surface geometry for the (1 1 0) surface of cubic ZnS (after Duke and Paton [54]).

Table 5. (1 1 0) surface geometry parameters (as shown in figure 2). All of the distances are in Å and the ω angle is in degrees.

	IP1	IP2	IP3	IP4	IP5	DFT ^{a,b}	exp. ^c
a_x	3.821	3.825	3.854	3.871	3.795		3.825
a_y	5.403	5.410	5.450	5.475	5.367		5.409
$\Delta_{1,\perp}$	-0.013	0.370	0.531	0.128	0.744	0.320, 0.55	0.59
$\Delta_{1,y}$	4.426	4.252	4.162	4.318	4.330	4.345, 4.21	4.296
$d_{12,y}$	2.871	2.947	2.997	2.887	3.197	3.006, 3.12	3.149
$d_{12,\perp}$	1.700	1.566	1.544	1.720	1.285	1.590, 1.49	1.403
$\Delta_{2,\perp}$	-0.009	0.094	0.091	0.031	0.058	0.072, 0.000	0.000
d_0	1.967	1.888	1.891	1.898	1.837	2.001, 1.87	1.912
ω_1	179.250	17.702	22.406	6.335	35.673	15.9	28.0

^a Ref. [14], ^b Ref. [15], ^c Ref. [54].

of zinc-blende ZnS in nature. Duke and Paton [54] studied atomic geometries of a (1 1 0) surface of ZnS using low-energy electron diffraction (LEED) analysis. The relaxed (1 0 0) surface structure and its structural parameters suggested by Duke and Paton is schematically shown in figure 2. Table 5 represents the ZnS(1 1 0) surface properties that are calculated by different potential formulations. The corresponding experimental and first principle values are represented where available.

The structural relaxation of different surfaces of II–VI semiconductors is well established by numerical and experimental studies. It has been observed that anions move outwards from the surface and cations move inwards [23]. It seems that all of the potentials, except IP1, can predict this surface reconstruction. This potential has also been used in other studies to calculate ZnS(1 1 0) properties [13, 31]. Unfortunately, we could not reproduce the results reported in these studies ($E_s = 0.53$ [13], 0.65 [31]; $\Delta_{1,\perp} = 0.42$ [13], 0.28 [31]). To check the accuracy of our calculations, we used the surface configuration already relaxed by IP2 potential as the input for IP1 surface calculations and we ended up with the same surface properties that are reported in table 5. The IP5 potential also predicts a less stable (1 1 0) surface, which is probably due to the fact that this potential does not consider charged species. The effect of the charges becomes more considerable when the system has free surfaces as coulomb forces acting on surface atoms that are not homogenous in three dimensions.

Table 6. A comparison of the surface energies (J/m^2) of ZnS in ZB and WZ structures, calculated using different empirical potentials (Zn and S denote Zn-terminated and S-terminated surfaces, respectively).

		IP1	IP2	IP3	IP4	IP5	DFT ^a
ZB							
(1 1 0)		0.825	0.515	0.439	0.554	1.176	0.43
(1 0 0)	Zn	1.845	1.532	1.161	1.111	1.773	2.03
(1 0 0)	S	1.724	1.295	1.038	1.121	1.652	2.03
(1 1 1)	Zn	1.369	0.851	0.676	0.856	1.513	1.36
(1 1 1)	S	1.407	0.981	0.863	0.897	1.418	1.36
WZ							
(0 0 0 1)	Zn	1.368	0.828	0.661	0.858	1.475	1.394
(0 0 0 1)	S	1.658	0.961	0.879	0.907	1.418	1.394
(1 0 $\bar{1}$ 0)		0.862	0.520	0.439	0.575	1.028	0.431
(1 1 $\bar{2}$ 0)		0.854	0.500	0.384	0.562	1.156	0.427

Ref. [3] for ZB and Ref. [5] for WZ surface energies.

In addition to the (1 1 0) surface of the ZB structure, we also studied the other most observed surfaces in ZB and WZ nanoparticles. The (1 0 0) and (1 1 1) surfaces are known to be probable facets in ZB nanostructures [3] as well as (0 0 0 1), (1 0 $\bar{1}$ 0) and (1 1 $\bar{2}$ 0) in WZ ones [5]. It should be taken into consideration that (1 0 0), (1 1 1) and (0 0 0 1) surfaces are polar surfaces, which inherently exhibit a dipole moment. The polar surfaces would be unstable, showing high surface energies, unless the dipoles are removed. In this study, the dipole moments were removed by forming surface vacancies with the same procedure that was described by Hamad *et al* [23]. Another important fact about polar surfaces is that they can be made by cleaving along Zn or S layers. As a result, we can end up with Zn or S terminated surfaces. Table 6 shows the calculated surface energies using empirical potentials and DFT calculations. The DFT results for ZB and WZ phases are taken from two works by Feigl *et al* [3, 5].

Table 6 shows that all of the empirical potentials and the DFT calculations predict the same trend in surface energies. (1 1 0) is the most stable surface in the ZB phase, followed by (1 1 1) and (1 0 0). In the WZ phase, (1 1 $\bar{2}$ 0) has the smallest energy but the difference between this surface and (1 0 $\bar{1}$ 0) energies is negligible, suggesting a similar stability for both surfaces.

5. Behaviour under pressure

As mentioned previously, ZnS can be found in two fourfold coordinated ($Z = 4$) crystal structures in nature: zinc-blende ($F\bar{4}3m$) and wurtzite ($P6_3mc$). The first and second neighbour distances in both structures are similar. As a result, there is a small difference between the unit cell volume of the two structures. There has been a considerable amount of theoretical and experimental studies showing that ZnS undergoes phase transformation from fourfold to sixfold rocksalt structure ($Fm\bar{3}m$) at high pressures. High pressure x-ray diffraction has shown that this transformation results in a large volume change (13–17%) in a pressure range from 12 to 18 GPa [40, 45, 55].

In this section, we will examine the ability of interatomic potentials to model ZnS under pressure by comparing high pressure lattice dynamic results with experiments. Enthalpy and volume per atom are calculated for three phases using the lattice dynamic code within

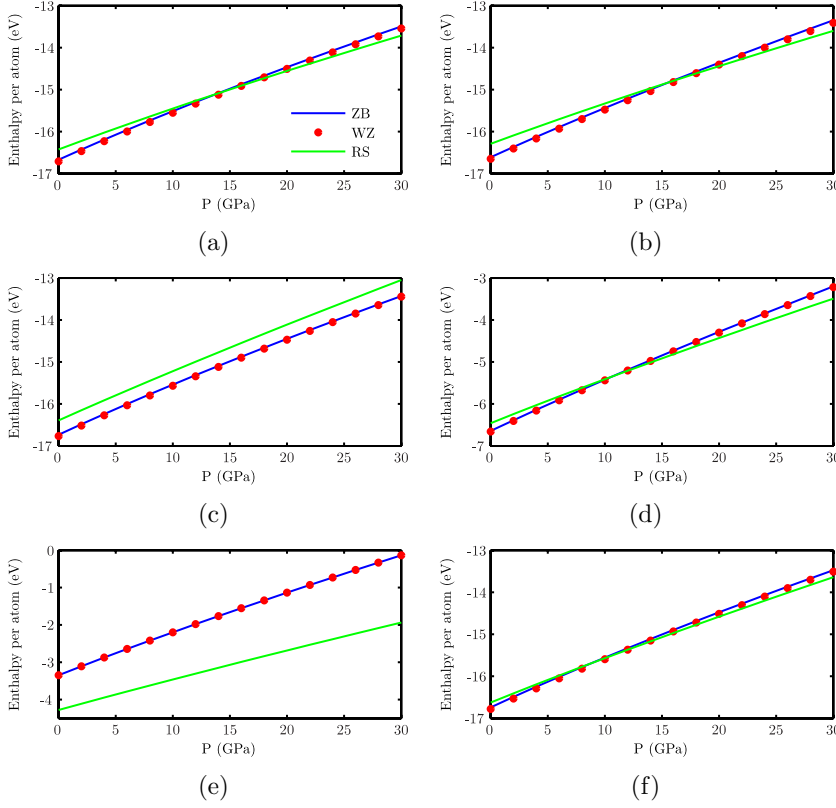


Figure 3. Enthalpy per atom as a function of pressure for bulk ZnS: (a) IP1, (b) IP2, (c) IP3, (d) IP4, (e) IP5 and (f) IP5 with the new 3bd cut-off.

GULP software. The coexistent pressure of fourfold and sixfold coordinated phases can be approximated by the point of equal enthalpy of both phases in figure 3.

Figure 3(e) clearly shows that IP5 potentials cannot model ZnS crystal structures correctly because rocksalt is more stable than zinc-blende and wurtzite at all pressures. This can be justified by the fact that IP5 potential does not consider the interaction between similar atoms. These interactions (especially anion–anion interactions) become more important in more condense phases, like rocksalt, where the atomic distances are smaller. The IP3 potential predicts that the rocksalt structure will be unstable at all pressures between 0 to 30 GPa. As shown in section 2, the mechanical properties of rocksalt that are calculated by the IP3 potential could be improved by changing the high three-body cut-off, as suggested in the original paper, to a smaller value. We expect that the ability of IP3 potential in modelling pressure induced phase transformation to be improved by changing the three-body cut-off as well. Figure 3(f) confirms that by changing the three-body cut-off to 3.0 Å the transition pressure calculated by IP3 lies in the range reported in experimental studies.

The relative volume change with increasing pressure is calculated for the four potentials that showed acceptable transition pressure values in figure 3. The resultant P – V graphs are plotted in figure 4 and compared with the three different experimental values.

Increasing pressure causes considerable divergence of wurtzite (and zinc-blende) relative volume from experimental values in figures 4(a) and (c). This is expected since the IP1

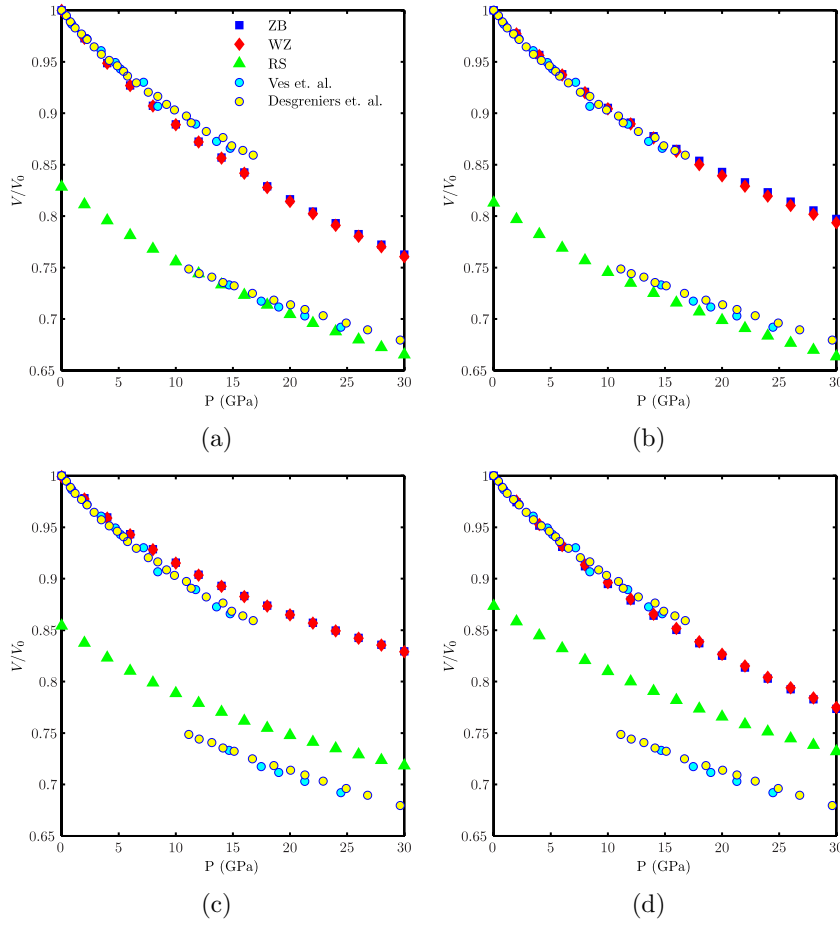


Figure 4. Pressure–volume relation of ZnS fourfold and sixfold phases for (a) IP1, (b) IP2, (c) IP4 and IP3 with the modified three-body cut-off potentials. The resultant graphs are compared with the experimental values of Ves *et al* [40] and Desgreniers *et al* [45].

and IP4 potentials underestimated and overestimated bulk modulus, respectively (table 1). The parameters of the equation of state (like the Murnaghan formulation) can be obtained by fitting to high density ZnS phase (rocksalt) experimental P – V data. The properties in ambient pressure can then be derived by extrapolation of the equation of state to 0 GPa. Using this method, relative volume of rocksalt to wurtzite phase (V_{RS}/V_{ZB}) in ambient pressure is reported to be 0.81 [40, 45]. The IP4 potential overestimates V_{RS}/V_{ZB} at ambient pressure, and this is the main reason for the large difference between calculated and experimental values in figure 4(c). This difference is larger in figure 4(d) since the IP3 potential overestimates both the relative volume and the bulk modulus of the rocksalt phase. Thus, even modifying the three-body cut-off cannot make this potential predict ZnS properties in high density structure accurately. Generally, it seems that the IP2 potential offers better modelling of ZnS under high pressure. The results of this section are summarized in table 7.

Table 7. Comparison of behaviour of four interatomic potentials of ZnS under pressure. V_T/V_0 , ΔV_T and P_T are relative volume, volume change and pressure of phase transformation, respectively.

	IP1	IP2	IP3 ^c	IP4	exp.
V_T/V_0	0.856	0.863	0.892	0.903	0.865 ^a , 0.853 ^b
ΔV_T (%)	14.3	17.0	9.6	13.8	16 ^a , 17 ^b
P_T (GPa)	14	16	10	12	14.7 ^a , 14.6 ^b

^a Ref. [40], ^b Ref. [45], ^c Modified three-body cut-off potential.

6. Thermal expansion

The ability of a force field to model a material at higher temperatures enables many opportunities to investigate high temperature phenomena in atomistic scales. One of the physical properties that can be readily calculated by MD is the volume change with respect to temperature. When the experimental values are available, thermal expansion calculated by MD can be used as one of the factors to verify the ability of a force field to model high temperatures.

Although there are a considerable number of studies on the crystal structure of ZnS at low temperatures, there is not much experimental data available above room temperature. There are two sets of published experimental data on ZnS thermal expansion: a neutron diffraction high temperature lattice parameter measurement by Moss *et al* [56] and a dilatometry linear expansion by Roberts *et al* [57].

In this section, we compare the thermal expansion of ZnS modelled with different potentials with experimental values. Nosé–Hoover isothermal–isobaric ensemble (NPT) at 0 GPa were used within DL.POLY code to calculate volume change with temperature of $6 \times 6 \times 6$ zinc-blende super cell with 3D periodic boundary condition. The final configuration of the simulation at each temperature is used as the initial configuration for the next simulation in order to accelerate the equilibration.

For the potentials containing a shell model, the adiabatic method that is described by Mitchell and Fincham [58] is used. In this method, the shell is given a small portion of ion mass and its motion is integrated by standard techniques. The shell mass should be small enough to ensure that the core–shell spring frequency is well above the vibrational frequencies of the lattice. From classical mechanics, the frequency of core–shell spring can be calculated as

$$\nu = \frac{1}{2\pi} \sqrt{\frac{k}{x(x-1)M}}, \quad (5)$$

where x is the fraction of the ion mass assigned to shell, M is the ion mass and k is the shell constant. Equation (5) shows that smaller shell constants require smaller shell masses to satisfy adiabatic conditions. Technically, this means that much smaller MD time steps are required to capture the fast movement of the light shells. In addition to slowing down the simulations, light shells are problematic at higher temperatures due to their much higher vibrational frequencies in respect to the lattice.

For sulfur, we chose $x = 0.1$, which results in core–shell frequencies of 48 THz and 34 THz for IP2 and IP3 potentials, respectively. These frequencies are well above the known vibration modes in ZnS. For the IP1 potential, we had to choose x as small as 0.01 to ensure that the zinc core–shell frequency is in the same range as sulfur. To keep consistency, a time step of 0.1 fs was used for all of the potentials and NPT simulations were run for 100 ps. Final lattice

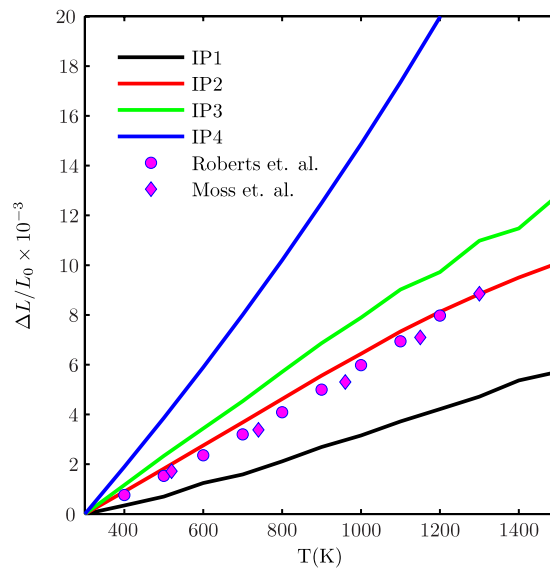


Figure 5. Thermal expansion of zinc-blende ZnS calculated by MD using different potential formulations. Experimental results are taken from Roberts *et al* [57] and Moss *et al* [61] works.

dimensions were calculated by taking the average of the last 10 ps of each simulation. It should be mentioned that we were unable to run MD simulations for the ZnS described by the IP5 potential. The system seems to be unstable at all high temperatures.

The temperature at which the zinc-blende to wurtzite phase transformation occurs is known to be around 1300 K (1273 [59], 1295 [60]). Moss *et al* also showed that ZnS keeps its complete cubic structure up to 1300 K [61]. The MD calculated and experimental values of thermal expansion are given in figure 5.

MD results should be treated with caution when they are used to calculate thermal expansion. The simulation cell should be equilibrated carefully and average cell dimensions should be calculated when the fluctuation in cell dimensions is in the same order of magnitude as thermal expansion. Considering this, it seems that the IP2 potential shows a better agreement with the experimental thermal expansion results. The thermal expansion behaviour of wurtzite is also calculated and it is seen to be fairly similar to zinc-blende for all potentials. The energy difference between the two phases is very small (about 0.5%) with a slightly more stable wurtzite in all temperatures.

7. Potential energy hypersurface

Derivation of force field parameters by fitting to a potential energy hypersurface obtained from first principle methods is one of the main ways to develop empirical interatomic potentials. An *ab initio* energy hypersurface is usually calculated by changing the geometry of periodic solids, gas phases, or both. The potential energy hypersurface that is calculated from a reliable first principle method can also be a good criterion to compare different empirical force fields.

In this section, we compare the energy hypersurfaces that are calculated using empirical potentials with those obtained from the density functional theory (DFT) calculations. Gaussian

optimized basis sets for ZnS by Heyd *et al* [62] and middle-range exchange–correlation hybrid of Henderson, Izmaylov, Scuseria and Savin (HISS) functional [63] were used in the periodic boundary condition code [64] within the GAUSSIAN program [65] to calculate the first principle energy hypersurface. The basis set and functional that we used in this study have shown reliable results in structural and band gap calculations of ZnS. We have also checked the reliability of our DFT calculations by calculating optimized lattice constants for all three ZnS phases, which were in a very good agreement with the experimental values ($a_{ZB} = 5.413$, $a_{WZ} = 3.3.828$, $c_{WZ} = 6.260$, $a_{RS} = 5.071$).

Two different strategies were used to calculate the potential energy hypersurfaces for ZnS in a zinc-blende crystal structure. In the first set of calculations, we constructed the potential energy hypersurface by changing the zinc-blende ZnS unit cell volume. The lattice constant was changed from 5 to 5.8 Å with 0.01 Å increments and potential energy calculated at each step. As shown in the previous sections, this range of volume change covers expansion, due to increasing the temperature from 0 to 2000 K, and compression, due to increasing the pressure from 0 to 30 GPa, for all empirical potentials. Since the absolute energy values calculated with DFT and interatomic potential methods cannot be compared directly, the energy difference is calculated for each method:

$$\Delta E = E - E_0, \quad (6)$$

where E is the potential energy calculated at each step and E_0 is the minimum energy of corresponding empirical potential or DFT calculation. Since the minimum of each potential formulation occurs at its equilibrium lattice constant, we shifted all of the minimums to the lattice constant that is calculated via DFT (which is a good choice because it has a good agreement with the experimental value). This enabled us to compare the curvature of each empirical potential energy hypersurface with the one calculated from DFT. Anharmonicity of the energy hypersurface is noticeable in figure 6 because the slope of diagram is bigger in the compression mode ($a < 5.41$ Å) compared to the expansion mode ($a > 5.41$ Å). The IP2 potential has better agreement with DFT energy calculations in compression mode, which can verify the more favourable results that we have obtained for this potential in section 5. In expansion mode, which can be related to the thermal expansion, IP2 and IP3 potentials exhibit a better fit to DFT results. This is again in agreement with the thermal expansion results that are calculated in section 6.

The uniform volume change of zinc-blende unit cell cannot include the effect of the three-body interaction in the empirical potential formulations because the value of S–Zn–S angle stays the same when lattice dimensions are changed uniformly in all directions. In addition, the effect of polarization cannot be captured with changing cubic unit cell volume uniformly because minimum energy always happens when the cores and shells occupy the same positions. In order to capture the effect of presence of three-body and shell model terms in empirical potential formulations, we have used another strategy to calculate the energy hypersurface for the zinc-blende ZnS unit cell. In this method, one Zn atom was moved from its equilibrium position in the zinc-blende unit cell, $(\frac{1}{4}a, \frac{1}{4}a, \frac{1}{4}a)$, towards and away from the S atom at (0,0,0) along [1,1,1] direction (a is the unit cell). To stay on [1,1,1] direction, the fractional position of a Zn atom should always have a format like (α, α, α) . To build the energy hypersurface, α was changed from 0.15 to 0.35 with 0.01 increments. In order to include the polarization of the core–shell units, all of the shells were allowed to relax at each step while the cores were fixed. Figure 7 shows the resultant energy hypersurfaces. Compared to figure 6, the energy hypersurfaces in figure 7 show more anharmonicity. The slope of the DFT energy hypersurface is much bigger in the first half of the diagram where $0.15 < \alpha < 0.25$. This part of the diagram is equivalent to moving a Zn atom from its equilibrium fractional position

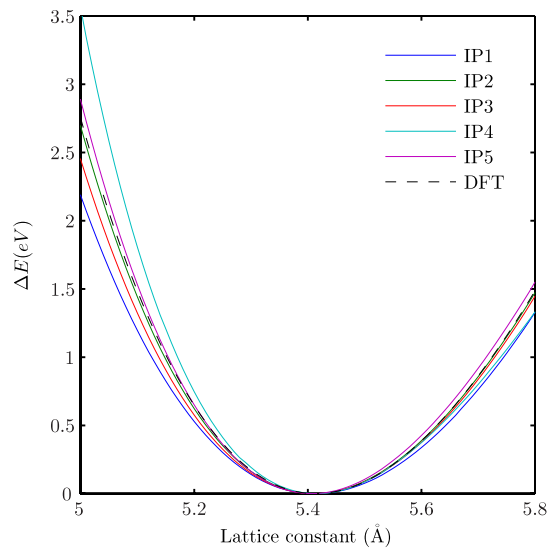


Figure 6. Energy hypersurfaces calculated via changing zinc-blende unit cell volume.

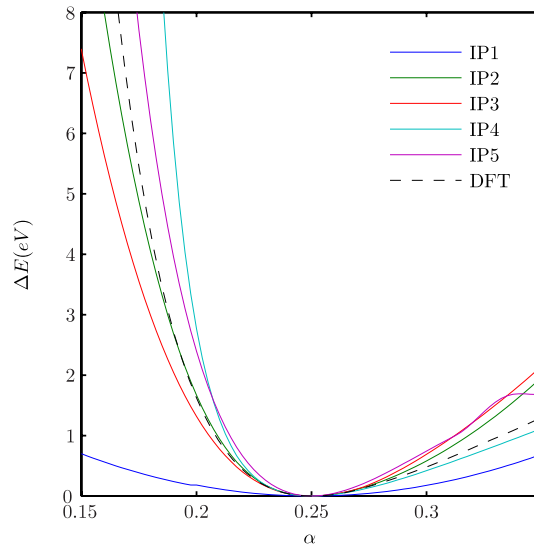


Figure 7. Energy hypersurfaces calculated via changing Zn atom fractional position (α, α, α) in a zinc-blende unit cell.

at $(0.25, 0.25, 0.25)$ towards the S atom placed at the origin. IP2 represents the best agreement with the DFT calculation in this region. Although IP2 diverges from DFT energy hypersurface in the second half of the figure 7, and IP4 fits better in this region, calculating the R^2 values showed that IP2 have the best overall agreement with the DFT results.

8. Conclusion

The performance of the five different empirical potentials for ZnS were tested and compared in this paper. This was done by calculating the different ZnS properties via empirical potentials

and then comparing them with the corresponding experimental results or DFT calculations. The properties tested in this paper are mechanical and structural properties, phonon dispersion relation, surface energy and structure, behaviour under pressure, thermal expansion and energy hypersurface. In section 2 we showed that lattice constants of ZB and WZ phases that are calculated by all of the empirical potentials are in acceptable agreement with the experiment. However, in the RS phase IP3 and IP5 could not reproduce the experimental lattice constant. This also happened for mechanical properties since the elastic constants calculated for the RS phase via IP3 and IP5 are very different from those calculated by the other three potentials. We have shown that mechanical and structural properties of RS phase calculated by IP3 potential can be improved by modifying its three-body cut-off distance.

The phonon dispersion relations for ZB and WZ phases were studied in section 3. Except for IP1, all of the other empirical potentials seemed to be able to reproduce the acoustic branch. All of the potentials showed weakness in predicting optical phonons. This was worse for IP5 since there was no LO/TO splitting due to the fact that atoms are charge neutral.

The surface properties of ZnS were studied in section 4. Previous theoretical and experimental studies showed that the (110) surface of ZnS experiences a considerable geometry change after relaxation. This surface relaxation includes the movement of anions to the out of the surface. This surface reconstruction was observed by all of the empirical potentials, except for IP1. The relaxed surface structures calculated by IP2 and IP3 were more similar to the experiment.

In section 5, IP1, IP2 and IP4 have been shown to be able to predict the pressure induced phase transformation. We have also shown that changing the three-body cut-off distance enables IP3 to show a pressure induced phase transformation. It was also observed that the P - V relation calculated by IP2 represents better agreement with the experimental results. The thermal expansion calculated by this potential has also shown better accordance to the experimental results. Finally, the energy hypersurface obtained from the DFT calculations has shown a better agreement to IP2 compared to the other empirical potentials.

Considering these results, we should emphasize that one general comment cannot be made on the reliability of particular empirical potentials. The choice of potential is highly dependent on the application that the molecular mechanic simulation aims for. Each of these potentials is designed to reproduce some specific ZnS properties. Except for IP5, we were able to run molecular dynamic simulations for temperatures as high as 1500 K. We noticed that more care should be taken when using potentials that include a shell model when running simulations at higher temperatures. Simulation speed is also highly dependent on the complexity of the potential formulation. Thus, potentials such as IP4 offer a much higher simulation speed than more complicated potentials, such as IP3.

Acknowledgments

MK, HZ, and QXL gratefully acknowledge the support of the Natural Sciences and Engineering Research Council of Canada (NSERC-CRD), Teck Metals Ltd and the Canadian Centre for Clean Coal/Carbon and Mineral Processing Technologies (C⁵MPT).

References

- [1] Qadri S B, Skelton E F, Dinsmore A D, Hu J Z, Kim W J, Nelson C and Ratna B R 2001 The effect of particle size on the structural transitions in zinc sulfide *J. Appl. Phys.* **89** 115
- [2] Feigl C, Russo S P and Barnard A S 2010 Safe, stable and effective nanotechnology: phase mapping of ZnS nanoparticles *J. Mater. Chem.* **20** 4971

- [3] Barnard A S, Feigl C A and Russo S P 2010 Morphological and phase stability of zinc blende, amorphous and mixed core-shell ZnS nanoparticles *Nanoscale* **2** 2294–301
- [4] Hamad S, Woodley S M and Catlow C R A 2009 Catlow experimental and computational studies of ZnS nanostructures *Mol. Simul.* **35** 1015–32
- [5] Feigl C A, Barnard A S and Russo S P 2012 Size- and shape-dependent phase transformations in wurtzite ZnS nanostructures *Phys. Chem. Chem. Phys.* **14** 9871–9
- [6] Zhang H, Huang F, Gilbert B and Banfield J F 2003 Molecular dynamics simulations, thermodynamic analysis, and experimental study of phase stability of zinc sulfide nanoparticles *J. Phys. Chem. B* **107** 13051–60
- [7] Akiyama T, Sano K and Nakamura K 2007 An empirical interatomic potential approach to structural stability of ZnS and ZnSe nanowires *Jpn. J. Appl. Phys.* **46**(4A) 1783–7
- [8] Zhang H, Rustad J R and Banfield J F 2007 Interaction between water molecules and zinc sulfide nanoparticles studied by temperature-programmed desorption and molecular dynamics simulations *J. Phys. Chem. A* **111** 5008–14
- [9] Feigl C A, Barnard A S and Russo S P 2012 Modelling nanoscale cubic ZnS morphology and thermodynamic stability under sulphur-rich conditions *CrystEngComm* **14** 7749
- [10] Grünwald M, Lutker K, Alivisatos A P, Rabani E and Geissler P L 2012 Metastability in pressure-induced structural transformations of CdSe/ZnS core/shell nanocrystals *Nano Lett.* **13** 1367–72
- [11] Mandal T, Maiti P K and Dasgupta C 2012 Mechanical properties of ZnS nanowires and thin films: microscopic origin of the dependence on size and growth direction *Phys. Rev. B* **86** 024101
- [12] Finkelstein N P 1997 The activation of sulphide minerals for flotation: a review *Int. J. Miner. Process.* **52** 81–120
- [13] Steele H M, Wright K and Hillier I H 2003 A quantum-mechanical study of the (1 1 0) surface of sphalerite (ZnS) and its interaction with Pb 2+ species *Phys. Chem. Miner.* **30** 69–75
- [14] Simpson D J, Bredow T, Chandra A, Cavallaro G P and Gerson A R 2011 The effect of iron and copper impurities on the wettability of sphalerite (1 1 0) surface *J. Comput. Chem.* **32** 2022–30
- [15] Jian-hua Chen, Ye Chen and Yu-qiong Li 2010 Quantum-mechanical study of effect of lattice defects on surface properties and copper activation of sphalerite surface *Trans. Nonferrous Met. Soc. China* **20** 1121–30
- [16] Porento M and Hirva P 2005 Effect of copper atoms on the adsorption of ethyl xanthate on a sphalerite surface *Surf. Sci.* **576** 98–106
- [17] Bag B, Das B and Mishra B K 2011 Geometrical optimization of xanthate collectors with copper ions and their response to flotation *Miner. Eng.* **24** 760–5
- [18] Foresman J B and Frisch A 1996 *Exploring Chemistry with Electronic Structure Methods: A Guide to Using Gaussian* (Pittsburgh, PA: Gaussian) 2nd edn
- [19] Sholl D and Steckel J A 2009 *Density Functional Theory: A Practical Introduction* (New York: Wiley-Interscience)
- [20] Grünwald M, Zayak A, Neaton J B, Geissler P L and Rabani E 2012 Transferable pair potentials for CdS and ZnS crystals *J. Chem. Phys.* **136** 234111
- [21] Tuckerman M E and Martyna G J 2000 Understanding modern molecular dynamics: techniques and applications *J. Phys. Chem. B* **104** 159–78
- [22] Wright K and Jackson R A 1995 Computer simulation of the structure and defect properties of zinc sulfide *J. Mater. Chem.* **5** 2037–40
- [23] Hamad S, Cristol S and Catlow R A 2002 Surface structures and crystal morphology of ZnS: computational study *J. Phys. Chem. B* **106** 11002–8
- [24] Wright K and Gale J 2004 Interatomic potentials for the simulation of the zinc-blende and wurtzite forms of ZnS and CdS: Bulk structure, properties, and phase stability *Phys. Rev. B* **70** 035211
- [25] Benkabou F, Aourag H and Certier M 2000 Atomistic study of zinc-blende CdS, CdSe, ZnS, and ZnSe from molecular dynamics *Mater. Chem. Phys.* **66** 10–16
- [26] Darden T, York D and Pedersen L 1993 Particle mesh Ewald: an Nlog(N) method for Ewald sums in large systems *J. Chem. Phys.* **98** 10089
- [27] Dick B G Jr and Overhauser A W 1958 Theory of the dielectric constants of alkali halide crystals *Phys. Rev.* **122** 90–103

- [28] Fan J 2011 *Multiscale Analysis of Deformation and Failure of Materials* (New York: Wiley)
- [29] Tersoff J 1986 New empirical model for the structural properties of silicon *Phys. Rev. Lett.* **56** 632–5
- [30] Tersoff J 1989 Modeling solid-state chemistry: interatomic potentials for multicomponent systems *Phys. Rev. B* **39** 5566–8
- [31] Wright K and Watson G W 1998 Simulation of the structure and stability of sphalerite (ZnS) surfaces *Am. Mineral.* **83** 141–6
- [32] Zhang H and Banfield J F 2004 Aggregation, coarsening, and phase transformation in ZnS nanoparticles studied by molecular dynamics simulations *Nano Lett.* **4** 713–18
- [33] Hamad S and Catlow C R A 2006 Computational study of the relative stabilities of ZnS clusters, for sizes between 1 and 4 nm *J. Cryst. Growth* **294** 2–8
- [34] Spanó E, Hamad S and Catlow C R A 2004 ZnS bubble clusters with onion-like structures *Chem. Commun.* 864–5
- [35] Hamad S, Cristol S and Catlow C R A 2005 Simulation of the embryonic stage of ZnS formation from aqueous solution *J. Am. Chem. Soc.* **127** 2580–90
- [36] Wright K 2009 The incorporation of cadmium, manganese and ferrous iron in sphalerite: insights from computer simulations *Can. Mineral.* **47** 615–23
- [37] Gale J D and Rohl A L 2003 The General Utility Lattice Program (GULP) *Mol. Simul.* **29** 291–341
- [38] Gao G, Van Workum K, Schall J D and Harrison J A 2006 Elastic constants of diamond from molecular dynamics simulations *J. Phys.: Condens. Matter* **18** S1737–50
- [39] Todorov I T, Smith W, Trachenko K and Dove M T 2006 DL_POLY_3: new dimensions in molecular dynamics simulations via massive parallelism *J. Mater. Chem.* **16** 1911
- [40] Ves S, Schwarz U, Christensen N E, Syassen K and Cardona M 1990 Cubic ZnS under pressure: optical-absorption edge, phase transition, and calculated equation of state *Phys. Rev. B* **42** 9113–18
- [41] Cohen M L and Chelikowsky J R 2012 *Electronic Structure and Optical Properties of Semiconductors (Springer Series in Solid-State Sciences)* (Berlin: Springer)
- [42] De Klerk J 1967 Elastic constants of α -ZnS *J. Phys. Chem. Solids* **28** 1831–7
- [43] Berlincourt D, Jaffe H and Shiozawa L R 1963 Electroelastic properties of the sulfides, selenides, and tellurides of zinc and cadmium *Phys. Rev.* **129**(3) 1009–17
- [44] Jamieson J C and Demarest H H Jr 1980 A note on the compression of cubic ZnS *J. Phys. Chem. Solids* **41** 963–4
- [45] Desgreniers S, Beaulieu L and Lepage I 2000 Pressure-induced structural changes in ZnS *Phys. Rev. B* **61** 8726–33
- [46] Cline C F 1967 Elastic Constants of Hexagonal BeO, ZnS, and CdSe *J. Appl. Phys.* **38** 1944
- [47] Uchida N 1972 Elastic and photoelastic constants of α -ZnS *J. Appl. Phys.* **43** 971
- [48] Chang E and Barsch G R 1973 Pressure dependence of single crystal elastic constants and anharmonic properties of wurtzite *J. Phys. Chem. Solids* **34** 1543–63
- [49] Cheng Y C, Jin C Q, Gao F, Wu X L, Zhong W, Li S H and Chu P K 2009 Raman scattering study of zinc blende and wurtzite ZnS *J. Appl. Phys.* **106** 123505
- [50] Lucovsky G, Martin R M and Burstein E 1971 Localized effective charges in diatomic crystals *Phys. Rev. B* **4** 251–62
- [51] Van Vechten J A 1969 Quantum dielectric theory of electronegativity in covalent systems: I. Electronic dielectric constant *Phys. Rev.* **182**(3) 181–905
- [52] Siqueiros J M, Machorro R and Regalado L E 1988 Determination of the optical constants of MgF(2) and ZnS from spectrophotometric measurements and the classical oscillator method *Appl. Opt.* **27** 2549–53
- [53] Parry D E 1975 The electrostatic potential in the surface region of an ionic crystal *Surf. Sci.* **49** 433–40
- [54] Duke C B 1984 The atomic geometries of GaP(1 1 0) and ZnS(1 1 0) revisited: a structural ambiguity and its resolution *J. Vac. Sci. Technol. A* **2** 515
- [55] Yang J, Zhu F, Zhang Q, Wu Y, Wu X, Qin S, Dong J-C and Chen D-L 2013 *In situ* XAFS investigation on zincblende ZnS up to 31.7 GPa *Chin. Phys. Lett.* **30** 046101

- [56] Moss B, McMullan R K and Koetzle T F 1980 Temperature dependence of thermal vibrations in cubic ZnS: a comparison of anharmonic models *J. Chem. Phys.* **73** 495
- [57] Roberts R B, White G K and Sabine T M 1981 Thermal expansion of zinc sulfide: 300–1300 K *Aust. J. Phys.* **34** 701–6
- [58] Mitchell P J and Fincham D 1993 Shell model simulations by adiabatic dynamics *J. Phys.: Condens. Matter* **5** 1031–8
- [59] Barlow D A 2013 Predicting the temperature for the solid–solid phase transition in II–VI semiconductor alloys *J. Phys. Chem. Solids* **74** 406–9
- [60] 2013 *CRC Handbook of Chemistry, Physics* 94th edn (Boca Raton, FL: CRC Press)
- [61] Moss B 1983 Comment on temperature dependence of thermal vibrations in cubic ZnS: a comparison of anharmonic models *J. Chem. Phys.* **78** 7503
- [62] Heyd J, Peralta J E, Scuseria G E and Martin R L 2005 Energy band gaps and lattice parameters evaluated with the Heyd–Scuseria–Ernzerhof screened hybrid functional *J. Chem. Phys.* **123** 174101
- [63] Lucero M J, Henderson T M and Scuseria G E 2012 Improved semiconductor lattice parameters and band gaps from a middle-range screened hybrid exchange functional *J. Phys. Condens. Matter* **24** 145504
- [64] Kudin K and Scuseria G 2000 Linear-scaling density-functional theory with Gaussian orbitals and periodic boundary conditions: Efficient evaluation of energy and forces via the fast multipole method *Phys. Rev. B* **61** 16440–53
- [65] Frisch D J *et al* 2009 Gaussian 09, Revision D.01